Impact of intragranular misorientation on void swelling and inter-granular cavities after ion irradiation in standard and additive manufacturing 316 L austenitic steels

Marie Loyer-Prost, Anne-Helene Puichaud, Camille Flament, Elodie Rouesne, Jean-Luc Bechade

Impact of intragranular misorientation on void swelling and inter-granular cavities after ion irradiation in standard and additive manufacturing 316 L austenitic steels

Marie Loyer-Prost[a,*], Anne-Hélène Puichaud[a], Camille Flament[a], E. Rouesne[b], Jean-Luc Béchade[a]

[a] Université Paris-Saclay, CEA, Service de Recherches de Métallurgie Physique, 91191, Gif-sur-Yvette, France.

[b] Université Paris-Saclay, CEA, Service de Recherches Métallurgies Appliquées, 91191, Gif-sur-Yvette, France.

[*]Corresponding author: Marie LOYER-PROST.

Mail: marie.loyer-prost@cea.fr

CEA Saclay, DES/ISAS/DMN/SRMP/JANNUS (Bât 126, pièce 58), PC. 162, 91191 Gif-sur-Yvette CEDEX, France.

+33 (0)1 69 08 24 68.

Highlights :

1. Standard and additive manufacturing 316L austenitic steels were ion irradiated
2. Loop density after irradiation strongly depends on the intra-granular misorientation
3. Void swelling of 316L steel starts with cavities near grain boundaries
4. Stereomicroscopy is a powerful methodology for loop nature determination
5. Dislocation loops were found to be interstitial type loops

Keywords:

Austenitic steels; Void swelling; Dislocation loop; Inter-granular cavity; Intra-granular misorientation

Graphical abstract

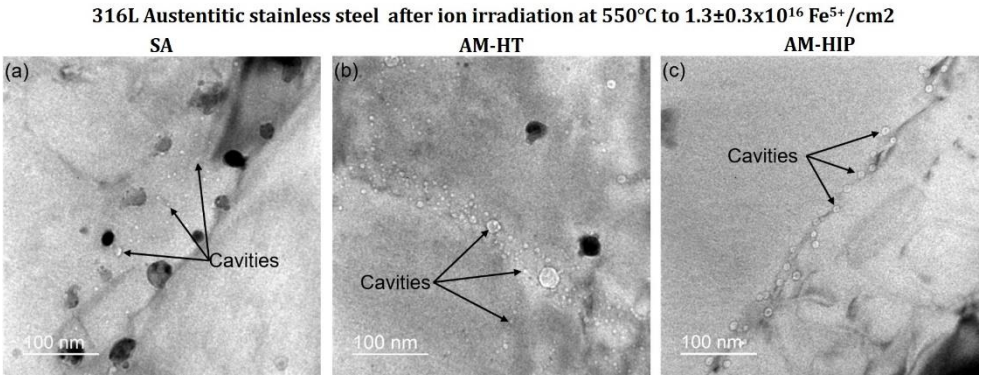

Abstract

Additive manufacturing (AM) is a promising technology for the design of materials with complex geometries with reduced cost and material waste. In order to be used in the nuclear industry, the capability of AM materials, in term of radiation resistance must be compared with materials elaborated in conventional ways. In this work, the radiation resistance of 316L austenitic stainless steels (ASSs) elaborated by AM is compared to a solution-annealed 316L ASS after irradiation with 5 MeV Fe^{5+} for 3 dpa at 550 °C (873 K). After irradiation, cavities are mainly located near grain boundaries for all studied alloys. Intra-granular cavities are only found in the AM material after heat treatment and are likely to be remaining porosity already present before irradiation. No cavities in intra-granular position are found in the conventional 316L ASS or in the AM material after hot isostatic pressing (HIP) at 1100 °C. It suggests that the void swelling ASSs starts by the formation of cavities at grain boundaries followed by a formation of cavities in intra-granular position, conventionally studied. Loops in the AM material with a hot treatment at 700°C are heterogeneously distributed due to a bimodal distribution of grains in terms of intra-granular misorientation. The intra-granular misorientation drastically reduces the loop density after irradiation. Frank and perfect loops are found to be only interstitial-type loops. The larger cavities' size and the more advanced dislocations network in the AM HIP sample suggests a slightly reduced radiation swelling resistance for the AM material but further investigations at higher irradiation dose have to be done.

1. Introduction

Additive manufacturing (AM) is a technology to fabricate objects based on a layer upon layer process. It is a promising methodology for many industrial fields as it allows to create complex geometries with a significant reduction in cost and material waste [1]. In particular, selective laser melting (SLM) gets a lot of attention by researchers for metals and alloys [2,3].

Austenitic stainless steels (ASSs) are used as structural materials in nuclear power plants due to its good corrosion resistance and mechanical properties [4]. AISI 316 ASSs constitute the baffle bolts in pressurized-water reactor (PWR) and are subjected to a high neutron flux and temperature ranging from 280 °C to 370 °C [5]. Advanced ASSs are also promising candidates for fuel cladding in GenIV fast neutron reactors operating at higher temperatures (400 °C – 650 °C) [6]. The microstructural evolutions of ASSs have been widely studied in the past after neutron [7–12], ion [5,13–15] and electron [16–18] irradiations at different temperatures with a particular interest given to their swelling [19]. It turns out that the initial metallurgical state, i.e. the density of dislocations induced by cold-working versus solution annealing, concentration in some addition elements as P, Cr or Ti [20], may impact the swelling [21]. According to Garner et al. [22] an incubation period is observed at low doses for which the microstructure evolves but the material does not swell. Thus the duration

of such period depends on the type of ASSs (metallurgical state, composition in addition elements). At higher doses, the material begins to swell with a quasi-constant gradient of 1%/dpa, independently of the type of ASS [6].

To date, quite little work has been done on irradiated 316L or 304L ASS materials fabricated by additive manufacturing [23–31]. The segregation of point defect clusters (vacancies and interstitials) which can evolve in dislocation loops and/or cavities affect the motion of dislocations. Their presence may impact the material's strength and ductility [32]. Moreover vacancies induced by irradiation may promote atomic diffusion behind segregation induced by irradiation or/and new phase formation. Irradiation defects clusters as dislocation loops and precipitates may contribute to the swelling of the steel under irradiation. Therefore the introduction of sinks for mobile point defects may be a way to develop swelling-resistant materials [33,34] but it will also affect the mechanical properties. Meric de Bellefon *et al.* showed that a high density of closely space twins leads to a higher resistance to void swelling [33].

Previous works [35,36] have shown that AM fabricated alloys usually present an as-built anisotropic microstructure with a high density of point defect sinks such as dislocations, solidification cells, grain boundaries, amorphous precipitates and also porosity. It has also been shown the strong effect of precursor material (composition of the powders…), but after irradiation samples with different composition evolve toward a similar state [30]. Thermomechanical treatments such as hot isostatic pressing (HIP) erase the porosity, reduce the columnar grains and solidification cells microstructure while they are preserved after stress-relieved heat treatments (HT). However in HIP AM fabricated 316L ASS, more precipitation is observed than in HT AM 316L ASS [36].

The global evaluation of radiation resistance of AM 316L ASSs compared to the conventional 316L ASS is complicated due to a large amount of metallurgical states studied in the literature (as built, thermally treated, HIP, …), with hardening effects depending on crystallographic anisotropic due to AM manufacturing process [29]. Therefore, the capability of AM materials is still in debate in the literature [28] and the global understanding of void swelling for AM materials is not yet completed. Depending on the studied AM materials and its conventional reference (annealed, forged or cold worked), some AM ASSs seem to have a better radiation resistance than conventional materials [23,31,37] and others lower [28]. For example, Shang, *et al* and Li, *et al.* reported that an as-built AM 316L ASS exhibits a lower dislocation loops density than a 70% cold worked 316L or a conventional coarse-grained 316L after irradiation in a temperature range from 450 °C to 600 °C. If Hou, *et al.* [38] and Sun, *et al.* [24] reported a lower helium swelling rate for an as-built AM 304L or an as-built AM 316L than conventional references (rolled 304L or forged 316L), Jiang et al. reported a higher void swelling for all studied AM 316 L ASSs (as-built, HIP) than the cold-worked (10 to 40% deformation) 316L materials studied [28]. Even if the cell structure dislocations induced by the AM process can serve as defect sinks [25,39] (thanks to high-density dislocation at cellular walls absorbing irradiation-

induced dislocation loops), they seems to be less efficient to annihilate radiation defects than the dislocations induced by the cold working [28].

The thermal treatment of AM materials after elaboration greatly influences the radiation tolerance of AM ASSs. Most studies agreed that a thermal treatment over 1100 °C or a HIP of AM materials will provide a better radiation resistance with a lower dislocation density and lower void swelling compared to the as-built material [23,25,27,28].

In addition to the difficult evaluation of the global radiation resistance of AM materials, the loop nature formed after irradiation (perfect and Franck loop nature, i.e. vacancy or interstitial) in AM 316L ASSs raises questions. Indeed Shang, *et al.* recently reported the co-existence of vacancy and interstitial loops in a 316L ASS irradiated with 3.5 MeV ions at 450°C [31] whereas Lin, *et al.* [26] reported only interstitial loops as usually found in conventional ASSs [40].

Regarding these different results, the influence of the initial microstructural state of AM 316 ASSs on the radiation damage needs some in-depth investigations such as the nature of the dislocation loops induced by irradiation. The conventional reference should also be careful considered. As neutron irradiations are long, costly and not easily accessible, ion irradiations are commonly used to screen the radiation resistance of materials. They provide a good control of all irradiation parameters (temperatures, flux and fluences).

In this study, 316L-type ASS cubes were fabricated by SLM using a commercial 316L powder. The AM fabricated materials were studied after: (i) a stress-relieved heat treatment (HT) and, (ii) a hot isostatic pressing (HIP) at 1100 °C for 3 h. The aim of this study is to determine the influence of heat treatment and hot isostatic pressure on the microstructure of AM fabricated 316L ASS after ion irradiation, for nuclear applications. The AM fabricated samples are compared to a cold-rolled 316L ASS annealed at 1100 °C for 30 min followed by quenching (SA 316L), which was subjected to the same ion irradiation. This paper is the first of a series that will describe the global evolution of microstructure of AM fabricated 316L ASS after ion irradiation. It focuses on the defects created by irradiation as dislocation loops and cavities, a second paper, for which analyses are in progress, will focus on chemistry and in particular the evolution of precipitates and the phenomenon of segregation under irradiation. Different techniques from transmission electron microscopy (TEM) were used to characterize the HT, HIP and SA 316L ASS.

2. Experimental procedure

2.1. Raw material

Samples were prepared from a commercial 316L ASS powder supplied by Trumpf GmbH. More details about the raw materials, the fabrication process and parameters and the heat treatments can be found elsewhere [36]. The reference is a cold-rolled, then solution annealed (SA) 316L ASS which was chosen for its close chemical composition to the AM samples (Table 1). The heat treatments are summarized in Table 2

Table 1: Chemical composition of the 316L raw powder and of the SA plate (in wt. %).

	Cr	**Ni**	**Mn**	**Si**	**Mo**	**C**	**N**	**O**	**S**	**P**	**Fe**
Trumpf 316L powder	17.55	11.75	1.15	0.45	2	0.018	0.088	0.023	0.007	≤0.001	Bal.
316L SA	17.44	12.33	1.82	0.46	2.3	0.024	0.060	-	0.001	0.027	Bal.

Table 2: Manufacturing conditions and heat treatment of the 316L ASS materials.

Sample references	**Manufacturing condition**	**Heat treatment**
SA	Cold-rolled	Solution annealed (1100 °C/30 min) followed by quenching
AM-As-built	AM	None
AM-HT	AM	Heat treatment 700°C hold for 1 h
AM-HIP	AM	Hot isostatic pressing 1100°C hold for 3 h at 1800 bars under argon

2.2. TEM Specimen preparation

Slices of the materials were mechanically thinned to approximately 100 μm using SiC grinding discs and 1 μm diamond paste finish. 3-mm discs were punched from these slices and thinned to electron transparency using a Tenupol-5 twin-jet electropolisher. The voltage for jet-polishing was set between 20-25 V, the electrolyte was a solution of 10 vol.% perchloric acid and 20 vol.% ether 2-butoxyethanol in ethanol and the temperature was maintained to 5°C.

2.1. TEM imaging

Microstructural examinations were performed using a Thermo Fischer Scientific Tecnai G20 transmission electron microscope (TEM) equipped with a LaB_6 filament operated at 200 kV and a charged coupled device camera for images and diffraction patterns acquisition. Samples thickness were measured using convergent-beam electron diffraction methods (CBED) [41] to calculate the density of cavities and dislocations after irradiation.

The cavities were observed in overfocused TEM micrographs. The micrographs were recorded for specimen tilted out of a zone axis to minimize the diffraction contrast created by the high density of dislocation loops and lines. The statistical analysis of the cavities and dislocation loops was determined by image analysis using Thermo Fischer Scientific Visilog Software.

The dislocation loop nature of the two type of loops formed in FCC materials: perfect and Frank loops, respectively with a Burgers vector of a/2<110> and a/3<111>, was identified using the classical inside-outside method within the First-Start/Right-Hand (FS/RH) convention [42] and/or the stereomicroscopy technic [43].

2.2. EBSD analysis

Electron backscattered diffraction (EBSD) analysis were performed to determine the mean misorientation inside the grains also called the Grain Orientation Spread (GOS). The GOS is the average of misorientation angles to the grain mean orientation. EBSD analysis were carried out on a Zeiss Sigma HD scanning electron microscope (SEM) operated at 20 kV equipped with a Bruker e-Flash HR detector. The step size was 0.47 µm. Data were post treated using the Bruker software Esprit. The mechanically polished samples were electropolished using a perchloric acid solution (70% ethanol, 20% ether-butoxyethanol, 10% perchloric acid) to remove irregularities and any deformation layer from the surface.

2.3. Irradiation

Ion irradiation were performed at the JANNuS-Saclay facility (Joint Accelerators for Nanoscience and Nuclear Simulation) using a 3 MV Pelletron accelerator [44]. Thin foil samples were irradiated at 823 K by 5 MeV Fe^{5+} ions at a mean flux of 1.75±0.4 x 10^{12} $Fe^{5+}.cm^{-2}.s^{-1}$. A high temperature of irradiation was chosen to be more representative of fast neutron reactors conditions. The fluence is estimated to be 1.3±0.3 x 10^{16} $ions.cm^{-2}$. The implanted Fe^{5+} ion depth at 5 MeV and the damage profile of displacement per atom (dpa) were calculated using Stopping and Range of Ions in Materials (SRIM2013) [45]. The Kinchin - Pease model was used for a quick damage estimate with a displacement threshold energy for Fe of 40 eV [ASTM E693]. The damage and implanted ions profiles are given in

Figure 1. A damage of 3 dpa was therefore observed in the first 200 nm of the samples.

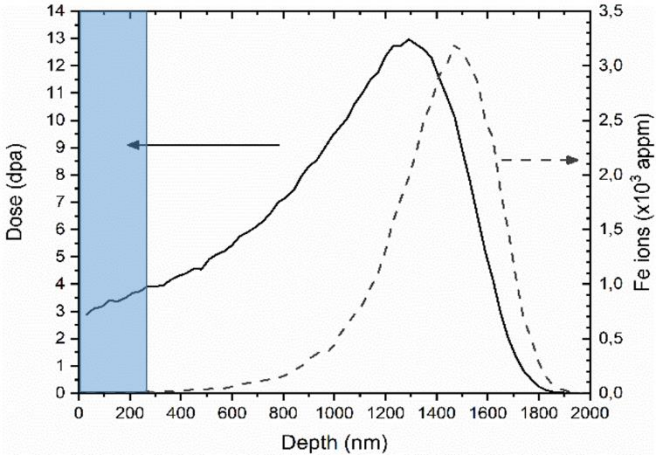

Figure 1: Evolution of the damage and the Fe^{5+} implantation depth, calculated using SRIM with Kinchin-Pease model. The observed area after is framed in blue.

3. Results

3.1. Microstructure before irradiation

The materials were thoroughly characterized before irradiation. The AM materials, before and after HT, present a strong epitaxial orientation in the <110> direction along the build direction (BD). The grains have an internal sub-cell structure defined by a high density of tangled dislocations, which disappears after HIP treatment. The EBSD maps reveal a stronger intra-granular misorientation for AM materials than SA ASS and a bimodal distribution of grains for the AM-HT ASS (Figure 2). Some grains of the AM-HT ASS have a strong intra-granular misorientation, higher than 20°, but most grains have a misorientation lower than 10°, such as all the grains in the SA and the AM-HIP ASSs. More details about the samples microstructure in terms of porosity and dislocation density before irradiation can be found elsewhere [36].

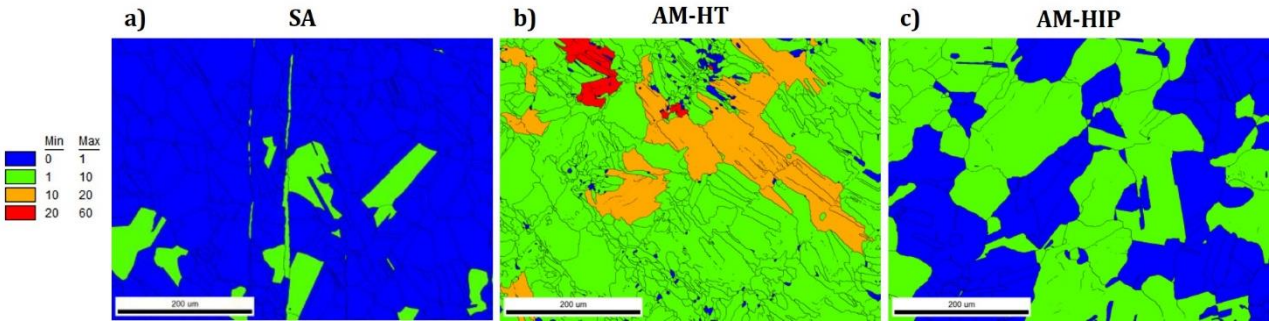

Figure 2: EBSD maps of the misorientation inside the grains also called the Grain Orientation Spread (GOS) for: (a) the cold-rolled SA, (b) the additive manufacturing 316L after heat treatment, AM-HT and (c) after hot isostatic pressure treatment, AM-HIP.

3.2. Microstructure after ion irradiation

3.2.1. Cavities

Voids are observed in all of the irradiated 316L and are heterogeneously distributed in the samples (Figure 3). Figure 4 shows the relative frequency of the cavities' apparent diameter and the mean diameter and density are summarized in Table 3.

Heterogeneous segregation of the cavities at grains boundaries (GBs), cell boundaries and around precipitates is observed in the three samples, as shown in Figure 3 (a, b and c). Almost no cavity is seen away from these sinks in the SA and HIP samples contrary to the HT sample where some cavities are seen inside the grains. In the reference SA sample, the apparent diameter of the cavities ranges between 2-34 nm, and 81 % of the cavities are smaller than 10 nm. The HT sample exhibits a high population of cavities smaller than 5 nm, as opposed to the SA and HIP samples. Those small cavities are segregated at grain and cell boundaries, and aligned along dislocation lines. Larger cavities (diameter > 40 nm) are also observed in the HT sample in

intragranular position and are likely to be remaining porosity that were already present before irradiation [32]. It has to be noted that they are facetted.

The HIP sample, which did not present any porosity before irradiation [36], presents cavities' size ranging between 2-20 nm. As opposed to the HT sample, no cavities with a diameter larger than 20 nm were observed and the cavities are heterogeneously distributed in the sample. In fact, they were only observed at grain boundaries, and none were observed within the grains or at twin boundaries.

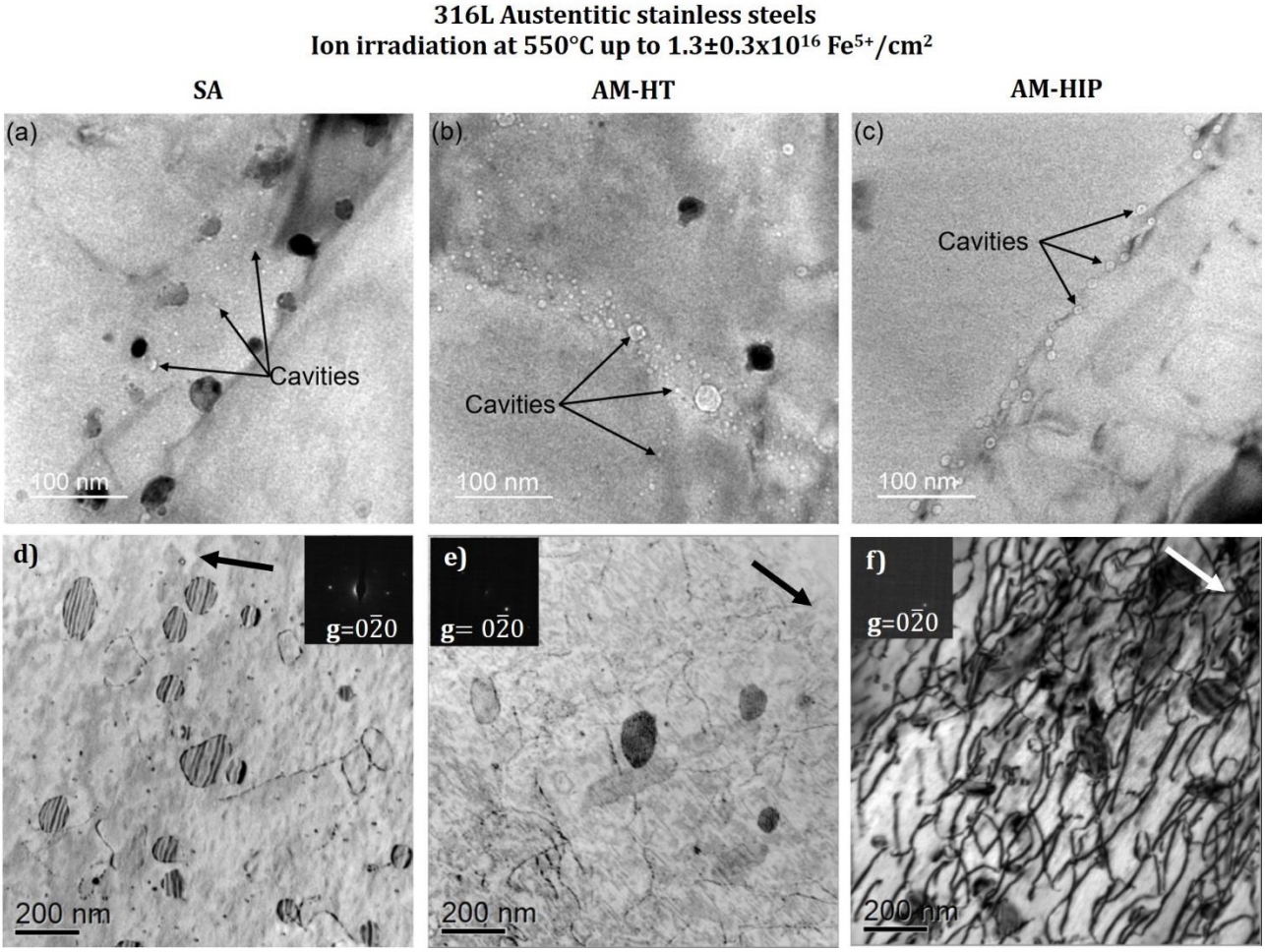

Figure 3: TEM micrographs of: (a, d) SA, (b, e) AM-HT, (c, f) AM-HIP 316L materials after 3 dpa irradiation, showing segregation of cavities at grain boundaries (a-c) and dislocation lines and loops (d-f).

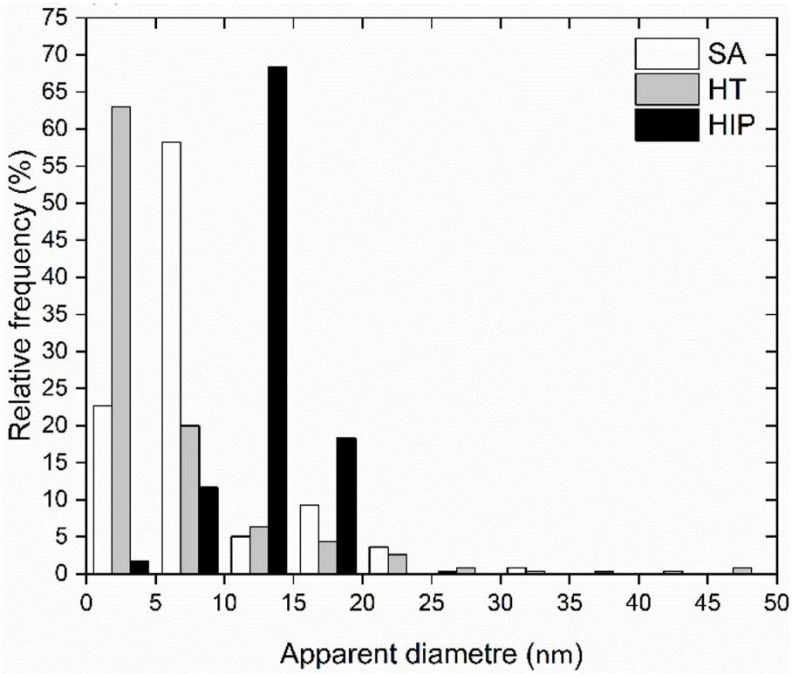

Figure 4: Relative frequency of the cavities diameter in AM 316L (HT and HIP) and SA specimen irradiated at 3 dpa.

Table 3: Mean apparent diameter (*d*) and density of the cavities, <111> dislocation loops and dislocation lines in 316L samples before [36] and after irradiation at 3 dpa. *After irradiation, the formation of cavities is very heterogeneous: they are located inside the grain boundaries; therefore the calculated density is the one near grain boundaries. Within the grains, the density would be near 0.

	Before irradiation			**3 dpa**				
	Cavities		**Lines**	**Cavities**		**Loops <111>**		**Lines**
	d	***ρ* ($10^{21}m^{-3}$)**	***ρ* ($10^{12}m^{-2}$)**	***d***	***ρ* ($10^{21}m^{-3}$)**	***d***	***ρ* ($10^{21}m^{-3}$)**	***ρ* ($10^{12}m^{-2}$)**
SA	not observed		<1	9.2 ± 0.4	0.6 ± 0.1*	73 ± 4	0.17 ± 0.01	7.9
AM HT	29 ± 1	0.12 ± 0.06	~10	7.1 ± 0.2	1.0 ± 0.3	120 ± 9	0.03 ± 0.01	50-67
AM HIP	not observed		1.3	12.3 ± 0.3	0.5 ± 0.1*	110 ± 7	0.10 ± 0.03	100

3.2.2. Dislocations

Before irradiation, only a few dislocation lines were observed in the SA 316L ASS, some remained in the not re-crystallised grains in the HIP sample, and all grains in the HT sample contained a high density of tangled dislocations [36].

After irradiation, a high density of dislocation lines and loops are observed. In all studied materials, both perfect loops with a Burgers vectors ½<110> and Frank loops with a Burgers vectors of 1/3<111> are observed. Frank loops (Figure 3 d-e-f) exhibit a fault contrast in their habit plane with a diffraction vector

{200} whereas perfect loops do not. Dislocation loops size and density are summarized in Table 3. Loops and lines are homogenously distributed in both SA 316L ASS and the AM HIP but they are heterogeneously distributed in the AM HT sample. Indeed some grains have almost no dislocation loops whereas other have a dislocation density comparable to the two others as one can see on Figure 5.

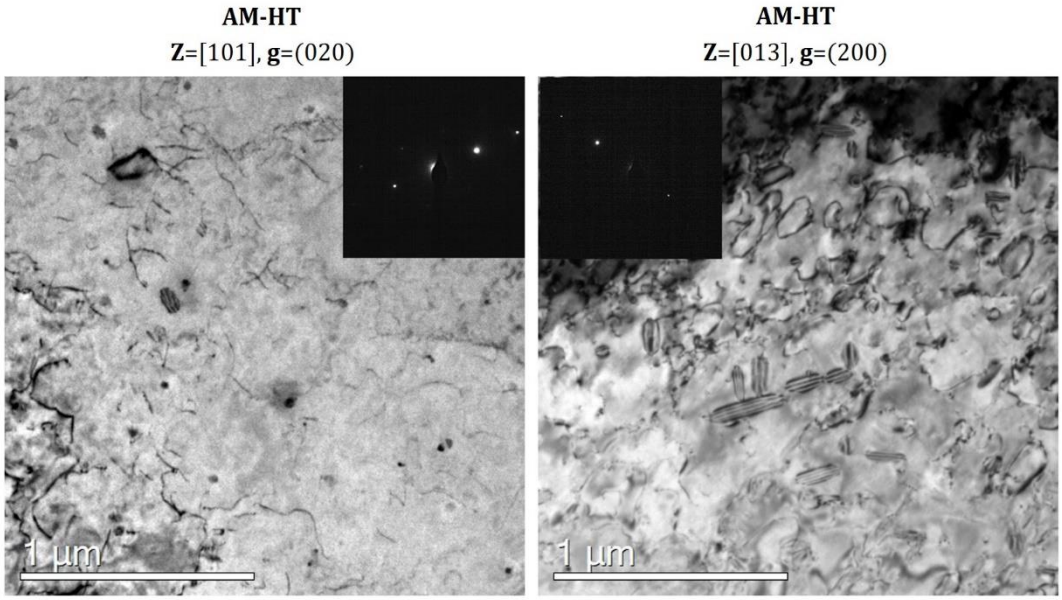

Figure 5: TEM micrographs of the AM-HT 316L alloy after 3 dpa ion-irradiation at 550 °C showing the heterogeneity of dislocation loop distribution between grains. Images are taken in Kinematic Bright Field conditions near the [101] zone axis and along the (020) diffraction vector (left) or near a [013] zone axis along the (200) (right). The first grain on the left exhibits only one dislocation loop and the second grain, on the right, has a higher dislocation density. The diffraction patterns of the micrographs are on the top corner for both images.

As the dislocation loop's nature in austenitic steels after ion-irradiation raises some questions in the literature, the nature of both perfect and Frank loops was identified using the stereomicroscopy technic with the First-Start/Right-Hand (FS/RH) convention in all samples [42].

The determination of the loop nature using the stereomicroscopy technic gives the same result as the conventional one as illustrated for the Frank loop circled in blue in Figure 6. The determination of loop nature by stereomicroscopy does not involve Burgers vector and the habit plane but only 2 parameters: the loop inclination versus the diffraction vector and the loop contrast (inside or outside). The loop inclination is identified by comparing the size of the loop in 2 TEM images taken with the same loop contrast for two foil inclinations.

The loop nature determination for both Frank loops and perfect loops for the SA 316L ASS is illustrated in Figure 6. The Frank loop circled in blue in Figure 6 (a) is out of contrast for the diffraction vectors $(\bar{2}02)$, $(02\bar{2})$ and $(2\bar{2}0)$ so its Burgers vector is $\pm 1/3[111]$. As it has an inside contrast for g=$(0\bar{2}0)$ (Figure 6 (a)) and outside contrast for (020) (Figure 6 (e)), the scalar product **g.b** is negative (<0) for g=$(0\bar{2}0)$ so its Burgers

vector is $1/3[111]$ in FSRH convention. As a Frank loop has always its normal to its habit plane (**n**) collinear to its Burgers vector, the sign of the scalar product **g.n** is the same as **g.Z** (with **Z** zone axis) and is positive. As **g.n**>0, in FSRH convention, the Frank loop is an interstitial type. The same nature is found using the stereomicroscopy technics [43]. By comparing the width of the blue loop between in Figure 6 (a) and (b), where it has an inside contrast, with respectively Figure 6 (e) and (f), where the loop has an outside contrast, the blue loop is larger for the lowest alpha tilt ((b) and (f)). Considering the rotation sense of alpha between the two images (indicated at the top of Figure 6), the orientation of the blue loop can be deduced and is illustrated in Figure 6 (a) and (i). For g=$(0\bar{2}0)$, the blue loop has an inside contrast so **g.b**<0. Considering, the loop orientation and the sense of the diffraction vectors, the Burgers vectors is pointing in the same direction as the normal to its habit plane (**b.n**>0). The blue loop is therefore an interstitial type. The same analysis can be done for the perfect loop circled in red in Figure 6 (a). As the red loop is larger is Figure 6 (a) and Figure 6 (e) than in Figure 6 (b) and Figure 6 (f), the right side of the loop is higher than the left size. The loop orientation is illustrated is Figure 6 (a) and (j). As the red loop has an outside contrast for g=$(0\bar{2}0)$, **g.b**>0 and the burgers vectors is pointing in the same direction as its normal to its habit plane. The perfect loop is therefore interstitial. The loop nature determination was run on dozens of loops and always gave the same result: both Frank loops and perfect loops are interstitial-type loops.

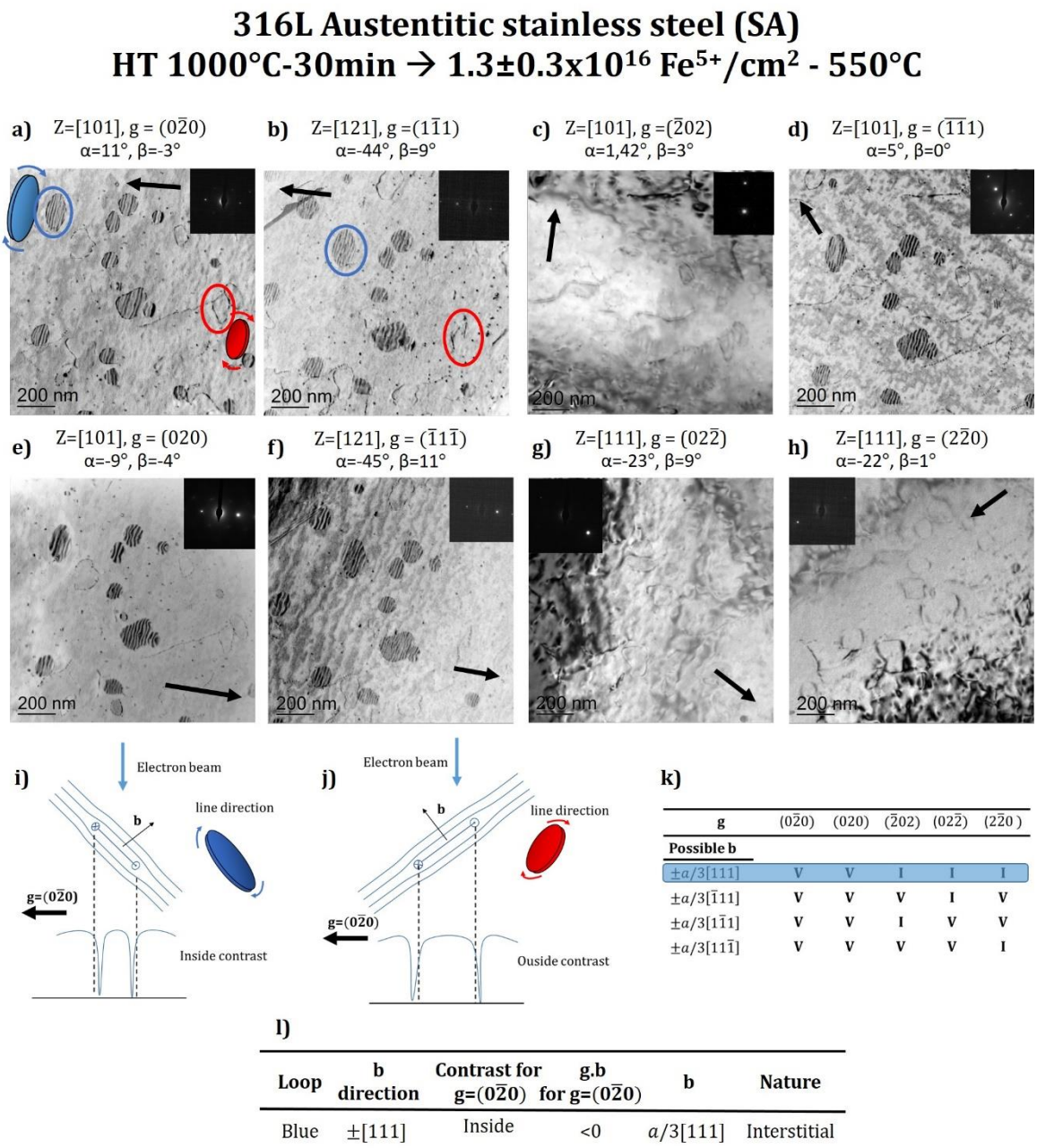

g	(0$\bar{2}$0)	(020)	($\bar{2}$02)	(02$\bar{2}$)	(2$\bar{2}$0)
Possible b					
$\pm a/3[111]$	V	V	I	I	I
$\pm a/3[\bar{1}11]$	V	V	V	I	V
$\pm a/3[1\bar{1}1]$	V	V	I	V	V
$\pm a/3[11\bar{1}]$	V	V	V	V	I

Loop	b direction	Contrast for g=(0$\bar{2}$0)	g.b for g=(0$\bar{2}$0)	b	Nature
Blue	±[111]	Inside	<0	$a/3[111]$	Interstitial

Figure 6: TEM micrographs of the SA 316L ASS after 3 dpa ion-irradiation at 550°C taking in weak beam dark field conditions for (a-b), (d-f) or kinematics bright field mode for (c), (g-h) in different diffraction conditions indicated above micrographs. The dark arrows on images (a-h) show the sense of diffraction vector selected for the micrographs and the diffraction patterns are in the corner of all images. The rotation sense of alpha tilt (when alpha increases) around the x axis for all micrographs is indicated above the micrograph (a). The schematic representation of a Frank loop circled in blue and perfect loop in red in (a) and (b) is superposed on image (a). The determination of the two loops' nature using stereomicroscopy in FSRH convention is illustrated in (i) and (j). (k) Table of Frank loops visibility for the used g of micrographs (a-h). (i) Determination of the nature of the Frank loop circled in blue in (a), using the convention method (Burgers vector determination and inside-outside contrast) in the FSRH convention.

Some loop nature determinations for the AM HT 316L ASS are illustrated for 4 Frank loops in Figure 7 and for two other loops in Figure 8. On the dozen of loops analysed, only one loop was found to be vacancy type. This loop is circled in green in Figure 8. In the Figure 8, the loops circled in blue and in green have both a

larger projection perpendicularly to the y axis for the highest β tilt (TEM micrograph in the middle). Their orientation towards the diffraction vector selected (020) is therefore identical. Nevertheless their inside-outside behaviour for g=(020) and $(0\bar{2}0)$ is the opposite. The loop circled in blue has an inside contrast for g=(020) (**g.b**>0**)** and is therefore an interstitial-type loop (**b.n**>0) and the loop is green has an outside contrast for g=(020) (**g.b**<0**)** and is therefore a vacancy-type loop.

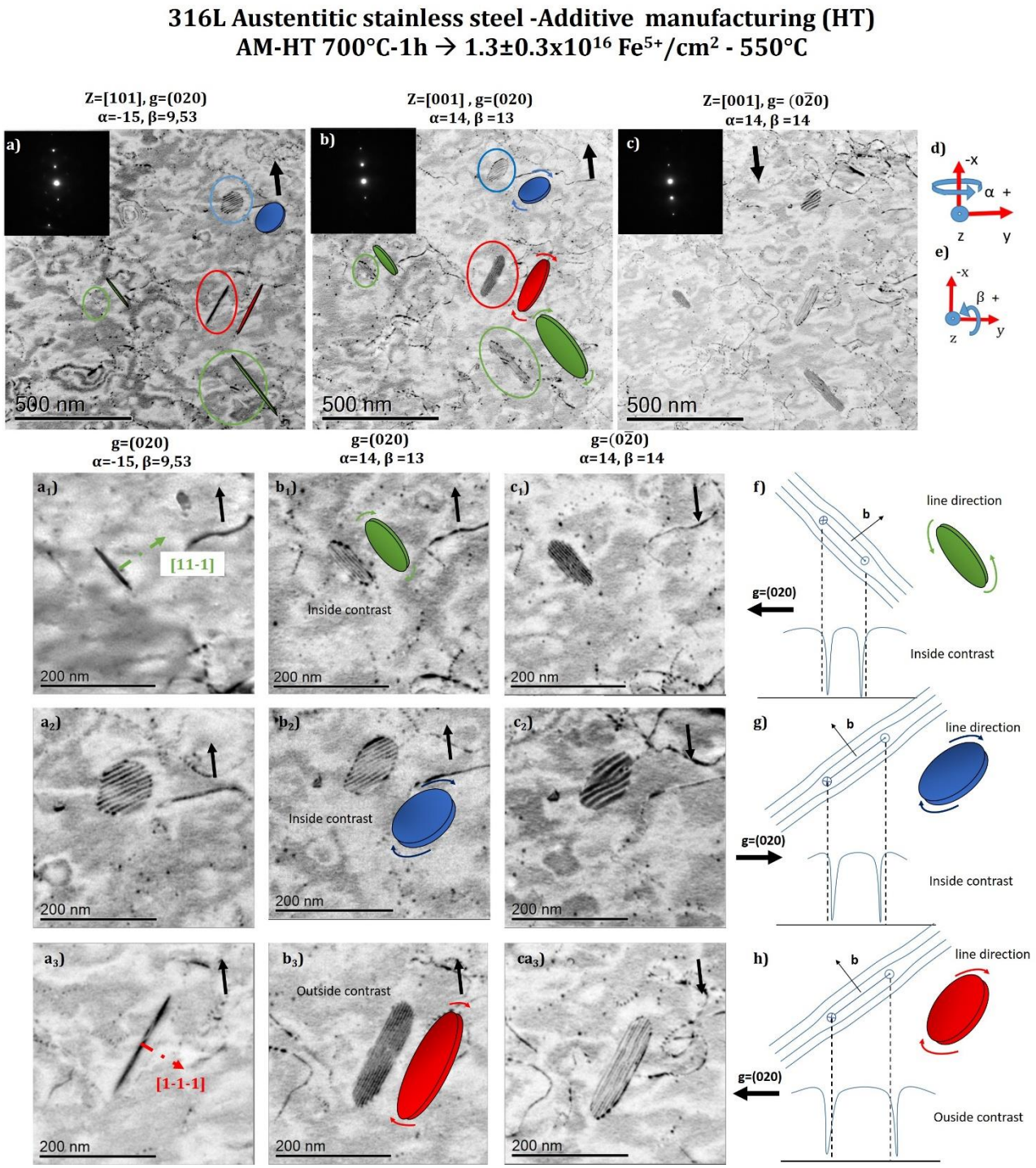

Figure 7: TEM micrographs of the AM HT 316L ASS after 3 dpa ion-irradiation at 550 °C taken in weak beam dark field conditions for (020) (a, a_1, a_2, a_3, b, b_1, b_2, b_3) and $(0\bar{2}0)$ (c, c_1, c_2, c_3) either close to a [101] or a [001] zone axis as indicated above the micrographs.

Images x_1, x_2, x_3 are enlargements of images x (x=a, b, c). The dark arrows on images show the sense of diffraction vector and the diffraction patterns are in the corner of images (a), (b), (c). The rotation sense of the α tilt (when α increases) and the rotation sense of the β tilt are indicated in (d) and (e). The determination of loop nature for 3 Frank loops circled in green, blue and red in figures (a, b) is illustrated in (f), (g), (h). The loop inclination and the direction of the diffraction vector are deduced from image (a_x) and (b_x).

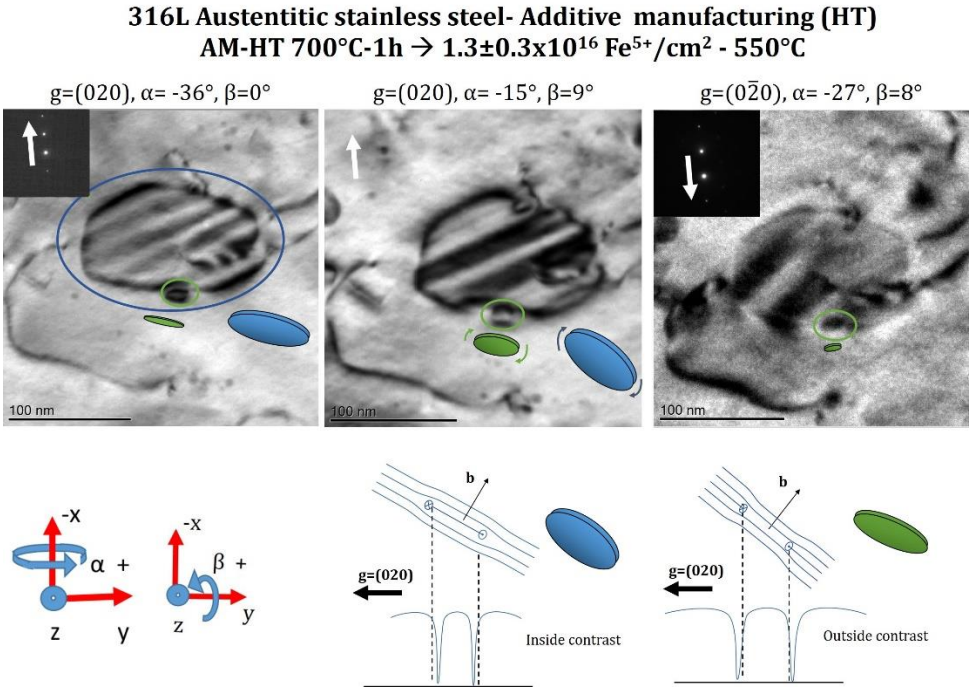

Figure 8: TEM micrographs of the AM HT 316L ASS after 3 dpa ion-irradiation at 550 °C taking in kinematic bright field conditions for (020) and (0$\bar{2}$0). The white arrows on the images show the sense of diffraction vector and the diffraction patterns are in the corner of images. The rotation sense of the α tilt (when α increases) and the rotation sense of the β tilt are indicated below TEM images. The orientation and nature of the two loops circled in blue and green are illustrated below the TEM images. The loop circled in blue is an interstitial type loop and the one circled in green is a vacancy-type loop.

The loop nature determination for the AM HIP 316L ASS is illustrated for 2 Frank loops and 2 perfect loops in Figure 9. The orientation of each 4 loops is deduced from the images (c) and (d) by comparing their size perpendicularly to the β tilt axis (vertical size) considering the sense of β rotation indicated in Figure 9 (f). The orientations of the 4 loops are indicated schematically in Figure 9 (g to j). The Burgers vector of the loops circled in blue and orange can even be deduced from their orientation and the stereogram in Figure 9(o). Indeed, their contrast in Figure 9(a) indicated that they are Frank loop with a $\frac{1}{3}$<111> type Burgers vector. Due to their orientation, the loop circled in orange has a Burgers vector of $\frac{1}{3}[111]$ and the one in blue $\frac{1}{3}[1\bar{1}1]$. The nature of the four loops is deduced from their orientation versus the diffraction vector and their inside-outside contrast. Each loop are interstitial-type loop as shown in Figure 9 (k to p).

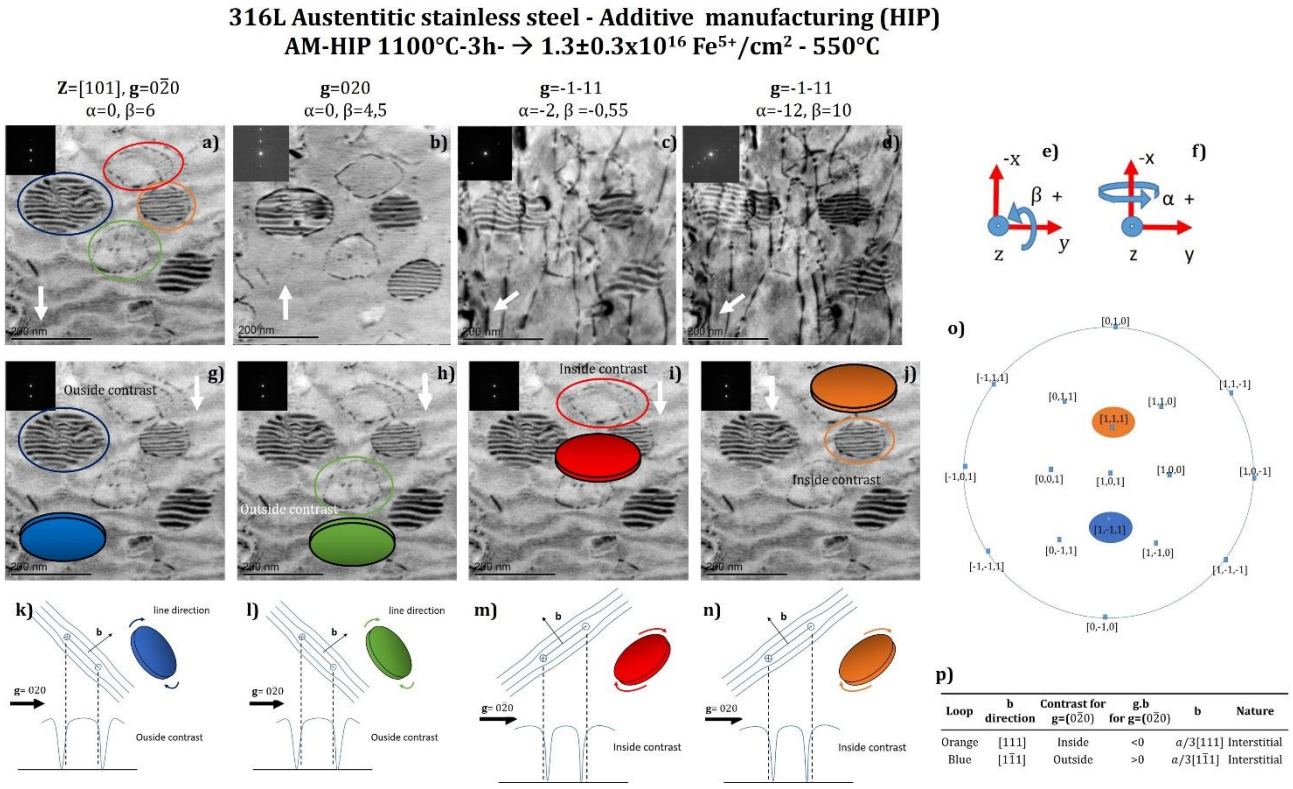

Figure 9: TEM micrographs of the AM HIP 316L ASS after 3 dpa ion-irradiation at 550 °C taking in kinematic bright field conditions (c and d) and weak beam dark field conditions (a, b, g-j) for (0$\bar{2}$0) (a, g-j), (020) (b), ($\bar{1}\bar{1}$1) (c and d). The white arrows on the images show the sense of diffraction vector and the diffraction patterns are in the corner of the images. The rotation sense of the α tilt (when α increases) and the rotation sense of the β tilt are indicated in (e and f). The stereogram of Ni in the [101] zone axis allowing to deduced the Burgers vector of the loops circled in blue and orange in (a). Table (p) indicates the nature of the loops circled in blue and orange taking into account their Burgers vector and their inside-outside behaviours.

To summarize, the interstitial nature of both perfect and Frank loops was identified by the First-Start/Right-Hand (FS/RH) method using stereomicroscopy technic in all samples. Only one vacancy-type loop was detected in the HT sample near an interstitial-type loop and is not representative of the global loop nature. Dislocation loops size and density are summarized in Table 3.

4. Discussions

4.1. Cavities

Interestingly, the average diameter of the cavities formed in our samples is significantly larger than the one reported for conventional 316L irradiated at the same temperature (550°C) and for approximately the same dose[14]. Jublot-Leclerc et al. reported a diameter around 2.5 nm for a 316L irradiated at 550°C and 4 dpa with 4 MeV Au^{2+} [14]. Here the average diameter of the cavities has a comparable size to the one reported in other AM 316L specimens irradiated at 500 °C but for higher doses [25,28]. Indeed, Meric De Bellefon et al. and Jiang et al. reported a size of cavities around 15 nm for a fully recrystallized sample [25] or a HIP sample [28] irradiated at 50 and 100 dpa. One can wonder why the studied samples here have such large cavities for such a low fluence (3 dpa). One explanation is the localization of the studied cavities: they are located at point defects' sinks (GBs, precipitates and dislocation walls). In the literature the studied cavities are in intra-granular position contrary to this study where almost no cavity are seen inside the grains (except for the AM HT sample). Few studies in the literature mentioned cavities at GBs [5,12,46] or near GBs [47] in austenitic steels. Sometimes these inter-granular cavities/porosities are considered to be sample preparation artefacts and are attributed to intergranular precipitates/oxides that were removed during electropolishing [12]. Here as the samples were irradiated as thin foils and had not intergranular cavities prior to irradiation, the cavities can not be considered as sample preparation artefact.

Interestingly, Ayanoglu et al. claimed that cavities should form preferentially in the vicinity of grain boundary [46]. Our results suggest that cavities first formed at sinks (GBs, dislocation and precipitates) before forming inside the grains. The size of the cavities at grain boundaries in other studies should be significantly larger than the one reported. The theory of cavity growth sits on the segregation of vacancies. The absorption energy of vacancies and interstitials by a cavity is identical. Therefore for cavities to grow, the absorption of interstitials towards other sinks than cavities, has to be stronger than the one of vacancies, which is the case for dislocation lines and loops. As grain boundaries (GBs) are a powerful sink for point defects, a large amount of vacancies are driven towards GBs. This might explain the formation of cavities in a first step at GBs followed by a formation in intra-granular position which are accounting for void swelling.

The only sample with intra-granular cavities is the AM HT sample. These intra-granular cavities are four times larger than the ones along GBs (average diameter of 30 nm compared to 7.2 nm) which is contrary to a two steps mechanism of cavity formation. Nevertheless, the cavities are likely to be the ones already present before irradiation [36]. They can either be induced by the SLM process or by the sample preparation (oxides falling out of the thin foil).

If we compare the SA and the AM HIP samples, the localization of the cavities is the same. The cavities are slightly larger in the AM HIP sample presuming a larger void swelling at higher dose that has to be confirmed

with future irradiation. One reason could be some argon trapping during the AM process that enhanced the cavity formation during irradiation.

4.2. Dislocation loops

A high density of dislocation loops and lines in the samples after irradiation are observed. Both faulted 1/3<111> Frank loops and 1/2<110> perfect loops are formed under irradiation at 550°C.

Under irradiation, the microstructure of FCC materials evolves, different type of defects are reported. At low dose, black dots appear and grow. The nature of these dots raise questions in the literature as they are too small to be clearly identified as loop [14]. Once these black dots have a certain size they are identified as Frank loops. Frank loops grow and unfault into perfect loops. As perfect loops can glide, they interact with other dislocation loops to formed dislocation lines and a network [6,19,48,49]. Once the network is formed the size and density of loops slightly reduce [50]. Void swelling of austenitic steels starts after a threshold dose at which the dislocation network reaches saturation [6,49]. Therefore, even if void swelling is related to cavity formation, it is also indirectly strongly linked to the formation of dislocations at low dose. For a same composition, a delay in the formation of dislocation loops and in the dislocation network might imply a delay in the cavity formation. Here, the lower density of Frank loops combined with a higher density of dislocation lines in the AM HIP sample compared to the SA sample seems to indicate a more advanced microstructure evolution for the HIP sample. It could be the sign that the radiation resistance of HIP sample is lower than the one of SA sample. Assuming the AM HIP and the SA samples would have the same density of saturation for the dislocation network, a more advanced dislocation network in the AM HIP sample would imply a lower threshold dose for void swelling for the AM HIP sample than the SA sample. This assumption has to be confirmed with a higher dose irradiation.

The low <111> dislocation loops' density of the AM HT material compared to AM-HIP and SA samples raises questions. It could be the sign of a low nucleation rate of <111> loops due to the high proportion of dislocation lines' density before irradiation. Low dose irradiations should be performed to check this hypothesis.

It is interesting to note that the distribution of loops in the AM HT sample is very heterogeneous. Indeed some grains exhibit a density of loops comparable to the AM HIP and SA samples whereas others have almost no loops (Figure 5). This strong heterogeneity can be understood considering the EBSD maps of the intra-granular misorientation and the fact that an initial dislocation network induced a lack of Frank loops after irradiation [48,51–53]. The dislocation network is a powerful sink for irradiation defects and enhanced their recombination. As a result, the initial dislocation network recovers [51–54] and the formation of Frank loops is inhibited up to dozens of dpa [51,52]. In this study, the EBSD maps of the AM-HT ASS in Figure 2 highlights the co-existence of two types of grains. One has an intra-granular misorientation lower than 10°, like AM - HIP and SA grains, and other with a strong intra-granular misorientation higher than 10°. As an intra-granular

misorientation is related to the density of dislocation lines/network [55–58], the low intra-granular misorientation grains behave like the HIP and the SA samples, i.e. they exhibit some dislocation loops. The high intra-granular misorientation grains with a high density of dislocation line induced by the AM process have almost no loops after irradiation. It is likely that the intra-granular misorientation enhanced the defect recombination. .

In all samples, dislocation loops are interstitial-type loops as predicted by the rate theory [59]. Only one vacancy type loop was found in the periphery of an interstitial-type loop. Urban et al. previously observed this phenomenon in irradiated nickel and supposed a stabilization of vacancy-type loops due to the compression induced by the interstitial-type loops [60].

5. Conclusions

316L ASS fabricated by additive manufacturing (AM) were ion irradiated at 550 °C up to 3 dpa and compared to a solution annealed 316L ASS. We found that in terms of cavity mean size, density and distribution, the HIP AM 316L presents very similar results to the SA 316L ASS material. The cavities were located at grain boundaries indicating the internal void swelling commonly studied in the literature did not start yet. Both of those samples were free of pores and presented similar grain size prior irradiation. On the other hand, the HT AM ASS sample shows a high density of cavities, mostly located at grain boundaries with a range of size from 2 to 80 nm but also inter-granular cavities likely to be the porosities already present before irradiation.

Our observations of cavities at grain boundaries and not inside grains for the AM HIP and SA 316L ASSs suggest that the void swelling of ASS starts by the formation of cavities at grain boundaries followed by a formation of cavities in intra-granular position.

In all samples, dislocation loops were found to be interstitial type loops. Considering the formation of <110> and <111> dislocation loops, it was found that the AM samples present similar densities as the reference sample after irradiation. However, the AM HIP material exhibits larger <111> dislocation loops and lines density than the reference sample. The more advanced dislocation network in the AM HIP sample suggests a slightly reduced radiation swelling resistance.

The AM HT microstructure is highly heterogeneously contrary to the SA and the AM HIP coming from a strong intra-granular misorientation heterogeneity. Grains with a high intra-granular misorientation seems to have very few dislocation lines and loops.

Further studies are required to understand the effect of those defects on mechanical properties, as well as the influence of precipitations formed under irradiation, which will be the purpose of a second paper in preparation.

Acknowledgments

The authors thank the JANNuS-Saclay CEA team for their welcome and for performing the irradiation experiments; they also thank Aziz Chniouel, Fernando Lomello, Pierre-François Giroux and Hicham Maskrot for providing the additively manufactured 316L steels and Alexandra Renault and Joel Malaplate for the discussion about ASS behavior under irradiation. This study was funded by Cross-Cutting Skills Program on Materials and Processes (Frédéric Schuster, CEA)

References

[1] H. Fayazfar, M. Salarian, A. Rogalsky, D. Sarker, P. Russo, V. Paserin, E. Toyserkani, A critical review of powder-based additive manufacturing of ferrous alloys: Process parameters, microstructure and mechanical properties, Materials & Design. 144 (2018) 98–128. https://doi.org/10.1016/j.matdes.2018.02.018.

[2] E.O. Olakanmi, R.F. Cochrane, K.W. Dalgarno, A review on selective laser sintering/melting (SLS/SLM) of aluminium alloy powders: Processing, microstructure, and properties, Progress in Materials Science. 74 (2015) 401–477. https://doi.org/10.1016/j.pmatsci.2015.03.002.

[3] L.-C. Zhang, H. Attar, Selective Laser Melting of Titanium Alloys and Titanium Matrix Composites for Biomedical Applications: A Review, Advanced Engineering Materials. 18 (2016) 463–475. https://doi.org/10.1002/adem.201500419.

[4] S. Şahin, M. Übeyli, A Review on the Potential Use of Austenitic Stainless Steels in Nuclear Fusion Reactors, Journal of Fusion Energy. 27 (2008) 271–277. https://doi.org/10.1007/s10894-008-9136-3.

[5] J. Malaplate, B. Michaut, A. Renault-Laborne, T. Jourdan, F. Dalle, J. Ribis, B. Radiguet, F. Sefta, B. Décamps, Characterization of ion irradiated microstructure and cavity swelling evolution up to high doses in austenitic stainless steels representative of PWR internals, Journal of Nuclear Materials. 517 (2019) 201–213. https://doi.org/10.1016/j.jnucmat.2019.02.006.

[6] F.A. Garner, 4.02 - Radiation Damage in Austenitic Steels, in: R.J.M. Konings (Ed.), Comprehensive Nuclear Materials, Elsevier, Oxford, 2012: pp. 33–95. https://doi.org/10.1016/B978-0-08-056033-5.00065-3.

[7] J.-L. Seran, J.M. Dupouy, Swelling of solution annealed 316 cladding in rapsodie and phenix, ASTM International, American Society for Testing and Materials, 1982. 10.1520/STP34335S.

[8] J.P. Foster, D.L. Porter, D.L. Harrod, T.R. Mager, M.G. Burke, 316 stainless steel cavity swelling in a PWR, Journal of Nuclear Materials. 224 (1995) 207–215.

[9] D.J. Edwards, E.P. Simonen, S.M. Bruemmer, Evolution of fine-scale defects in stainless steels neutron-irradiated at 275 °C, Journal of Nuclear Materials. 317 (2003) 13–31. https://doi.org/10.1016/S0022-3115(03)00002-3.

[10] A. Renault Laborne, P. Gavoille, J. Malaplate, C. Pokor, B. Tanguy, Correlation of radiation-induced changes in microstructure/microchemistry, density and thermo-electric power of type 304L and 316 stainless steels irradiated in the Phénix reactor, Journal of Nuclear Materials. 460 (2015) 72–81. https://doi.org/10.1016/j.jnucmat.2015.02.014.

[11] A. Renault-Laborne, J. Garnier, J. Malaplate, P. Gavoille, F. Sefta, B. Tanguy, Evolution of microstructure after irradiation creep in several austenitic steels irradiated up to 120 dpa at 320 °C, Journal of Nuclear Materials. 475 (2016) 209–226. https://doi.org/10.1016/j.jnucmat.2016.04.020.

[12] A. Renault-Laborne, J. Hure, J. Malaplate, P. Gavoille, F. Sefta, B. Tanguy, Tensile properties and deformation microstructure of highly neutron-irradiated 316 stainless steels at low and fast strain rate, Journal of Nuclear Materials. 508 (2018) 488–504. https://doi.org/10.1016/j.jnucmat.2018.05.068.

[13] A. Etienne, M. Hernández-Mayoral, C. Genevois, B. Radiguet, P. Pareige, Dislocation loop evolution under ion irradiation in austenitic stainless steels, Journal of Nuclear Materials. 400 (2010) 56–63. https://doi.org/10.1016/j.jnucmat.2010.02.009.

[14] S. Jublot-Leclerc, X. Li, L. Legras, M.-L. Lescoat, F. Fortuna, A. Gentils, Microstructure of Au-ion irradiated 316L and FeNiCr austenitic stainless steels, Journal of Nuclear Materials. 480 (2016) 436–446. https://doi.org/10.1016/j.jnucmat.2016.08.006.

[15] B. Michaut, T. Jourdan, J. Malaplate, A. Renault-Laborne, F. Sefta, B. Décamps, Cluster dynamics modeling and experimental investigation of the effect of injected interstitials, Journal of Nuclear Materials. 496 (2017) 166–176. https://doi.org/10.1016/j.jnucmat.2017.09.018.

[16] K. Nakata, Y. Katano, I. Masaoka, K. Shiraishi, Grain boundary migration during electron irradiation in austenitic stainless steels, Journal of Nuclear Materials. 133–134 (1985) 575–579. https://doi.org/10.1016/0022-3115(85)90213-2.

[17] J. Sun, J. Qian, Z. Zhao, J. Chen, Z. Xu, Electron irradiation damage in austenitic stainless steels, Journal of Nuclear Materials. 179–181 (1991) 526–528. https://doi.org/10.1016/0022-3115(91)90141-S.

[18] J.P. Qian, L.P. Lu, J.M. Chen, J.G. Sun, Z.Y. Zhao, The influence of temperature on swelling behavior in electron irradiated austenitic stainless steels, Journal of Nuclear Materials. 191–194 (1992) 1229–1233. https://doi.org/10.1016/0022-3115(92)90670-G.

[19] F.A. Garner, Evolution of microstructure in face-centered cubic metals during irradiation, Journal of Nuclear Materials. 205 (1993) 98–117. https://doi.org/10.1016/0022-3115(93)90076-B.

[20] I.M. Neklyudov, V.N. Voyevodin, Radiation swelling of modified austenitic steels, Russian Physics Journal. 51 (2008) 400–413. https://doi.org/10.1007/s11182-008-9063-9.

[21] E.A. Kenik, J.T. Busby, Radiation-induced degradation of stainless steel light water reactor internals, Materials Science and Engineering: R: Reports. 73 (2012) 67–83. https://doi.org/10.1016/j.mser.2012.05.002.

[22] F.A. Garner, M.B. Toloczko, B.H. Sencer, Comparison of swelling and irradiation creep behavior of fcc-austenitic and bcc-ferritic/martensitic alloys at high neutron exposure, Journal of Nuclear Materials. 276 (2000) 123–142. https://doi.org/10.1016/S0022-3115(99)00225-1.

[23] M. Song, M. Wang, X. Lou, R.B. Rebak, G.S. Was, Radiation damage and irradiation-assisted stress corrosion cracking of additively manufactured 316L stainless steels, Journal of Nuclear Materials. 513 (2019) 33–44. https://doi.org/10.1016/j.jnucmat.2018.10.044.

[24] X. Sun, F. Chen, H. Huang, J. Lin, X. Tang, Effects of interfaces on the helium bubble formation and radiation hardening of an austenitic stainless steel achieved by additive manufacturing, Applied Surface Science. 467–468 (2019) 1134–1139. https://doi.org/10.1016/j.apsusc.2018.10.268.

[25] G. Meric de Bellefon, K.M. Bertsch, M.R. Chancey, Y.Q. Wang, D.J. Thoma, Influence of solidification structures on radiation-induced swelling in an additively-manufactured austenitic stainless steel, Journal of Nuclear Materials. 523 (2019) 291–298. https://doi.org/10.1016/j.jnucmat.2019.06.012.

[26] J. Lin, F. Chen, X. Tang, J. Liu, S. Shen, G. Ge, Radiation-induced swelling and hardening of 316L stainless steel fabricated by selected laser melting, Vacuum. 174 (2020) 109183. https://doi.org/10.1016/j.vacuum.2020.109183.

[27] M. McMurtrey, C. Sun, R.E. Rupp, C.-H. Shiau, R. Hanbury, N. Jerred, R. O'Brien, Investigation of the irradiation effects in additively manufactured 316L steel resulting in decreased irradiation assisted stress corrosion cracking susceptibility, Journal of Nuclear Materials. 545 (2021) 152739. https://doi.org/10.1016/j.jnucmat.2020.152739.

[28] L. Jiang, M. Song, L. Yang, J. Yang, D. Du, X. Lou, Y. Chen, A comparison study of void swelling in additively manufactured and cold-worked 316L stainless steels under ion irradiation, Journal of Nuclear Materials. 551 (2021) 152946. https://doi.org/10.1016/j.jnucmat.2021.152946.

[29] J.A. Evans, S.A. Anderson, E.J. Faierson, D. Perez-Nunez, S.M. McDeavitt, Anisotropic Radiation-Induced Changes in Type 316L Stainless Steel Rods Built by Laser Additive Manufacturing, Nuclear Technology. 205 (2019) 563–581. https://doi.org/10.1080/00295450.2018.1502001.

[30] B.P. Eftink, J.S. Weaver, J.A. Valdez, V. Livescu, D. Chen, Y. Wang, C. Knapp, N.A. Mara, S.A. Maloy, G.T. Gray, Proton irradiation and characterization of additively manufactured 304L stainless steels, Journal of Nuclear Materials. 531 (2020) 152007. https://doi.org/10.1016/j.jnucmat.2020.152007.

[31] Z. Shang, C. Fan, J. Ding, S. Xue, A. Gabriel, L. Shao, T. Voisin, Y.M. Wang, T. Niu, J. Li, T.D. de la Rubia, H. Wang, X. Zhang, Heavy ion irradiation response of an additively manufactured 316LN stainless steel, Journal of Nuclear Materials. 546 (2021) 152745. https://doi.org/10.1016/j.jnucmat.2020.152745.

[32] F.A. Garner, M.L. Hamilton, N.F. Panayotou, G.D. Johnson, The microstructural origins of yield strength changes in aisi 316 during fission or fusion irradiation, Journal of Nuclear Materials. 104 (1981) 803–807. https://doi.org/10.1016/0022-3115(82)90698-5.

[33] G. Meric de Bellefon, I.M. Robertson, T.R. Allen, J.-C. van Duysen, K. Sridharan, Radiation-resistant nanotwinned austenitic stainless steel, Scripta Materialia. 159 (2019) 123–127. https://doi.org/10.1016/j.scriptamat.2018.09.030.

[34] I.J. Beyerlein, A. Caro, M.J. Demkowicz, N.A. Mara, A. Misra, B.P. Uberuaga, Radiation damage tolerant nanomaterials, Materials Today. 16 (2013) 443–449. https://doi.org/10.1016/j.mattod.2013.10.019.

[35] T. Niendorf, S. Leuders, A. Riemer, H.A. Richard, T. Tröster, D. Schwarze, Highly Anisotropic Steel Processed by Selective Laser Melting, Metallurgical and Materials Transactions B. 44 (2013) 794–796. https://doi.org/10.1007/s11663-013-9875-z.

[36] A.-H. Puichaud, C. Flament, A. Chniouel, F. Lomello, E. Rouesne, P.-F. Giroux, H. Maskrot, F. Schuster, J.-L. Béchade, Microstructure and mechanical properties relationship of additively manufactured 316L stainless steel by selective laser melting, EPJ Nuclear Sci. Technol. 5 (2019). https://doi.org/10.1051/epjn/2019051.

[37] S. Li, J. Hu, W.-Y. Chen, J. Yu, M. Li, Y. Wang, Evolution of cellular dislocation structures and defects in additively manufactured austenitic stainless steel under ion irradiation, Scripta Materialia. 178 (2020) 245–250. https://doi.org/10.1016/j.scriptamat.2019.11.036.

[38] J. Hou, B. Dai, Y. Li, J. Zhao, Z. Chen, D. Pan, Y. Zhu, K. Zhang, A. Huang, Helium bubble nucleation in Laser Powder Bed Fusion processed 304L stainless steel, Journal of Nuclear Materials. 542 (2020) 152443. https://doi.org/10.1016/j.jnucmat.2020.152443.

[39] Z. Shang, C. Fan, S. Xue, J. Ding, J. Li, T. Voisin, Y. Wang, H. Wang, X. Zhang, Response of solidification cellular structures in additively manufactured 316 stainless steel to heavy ion irradiation: an in situ study, Materials Research Letters. 7 (2019) 290–297. https://doi.org/10.1080/21663831.2019.1604442.

[40] M. Suzuki, A. Sato, T. Mori, J. Nagakawa, N. Yamamoto, H. Shiraishi, In situ deformation and unfaulting of interstitial loops in proton-irradiated steels, Philosophical Magazine A. 65 (1992) 1309–1326. https://doi.org/10.1080/01418619208205606.

[41] P.M. Kelly, A. Jostsons, R.G. Blake, J.G. Napier, The determination of foil thickness by scanning transmission electron microscopy, Physica Status Solidi (a). 31 (1975) 771–780. https://doi.org/10.1002/pssa.2210310251.

[42] M.L. Jenkins, Characterisation of radiation-damage microstructures by TEM, Journal of Nuclear Materials. 216 (1994) 124–156. https://doi.org/10.1016/0022-3115(94)90010-8.

[43] J.W. Edington, Interpretation of Transmission Electron Micrographs, in: J.W. Edington (Ed.), Interpretation of Transmission Electron Micrographs, Macmillan Education UK, London, 1975: pp. 1–112. https://doi.org/10.1007/978-1-349-02658-6_1.

[44] L. Beck, Y. Serruys, S. Miro, P. Trocellier, E. Bordas, F. Leprêtre, D. Brimbal, T. Loussouarn, H. Martin, S. Vaubaillon, S. Pellegrino, D. Bachiller-Perea, Ion irradiation and radiation effect characterization at the JANNUS-Saclay triple beam facility, Journal of Materials Research. 30 (2015) 1183–1194. https://doi.org/10.1557/jmr.2014.414.

[45] J.F. Ziegler, M.D. Ziegler, J.P. Biersack, SRIM – The stopping and range of ions in matter (2010), Nuclear Instruments and Methods in Physics Research Section B: Beam Interactions with Materials and Atoms. 268 (2010) 1818–1823. https://doi.org/10.1016/j.nimb.2010.02.091.

[46] M. Ayanoglu, A.T. Motta, Microstructural evolution of the 21Cr32Ni model alloy under irradiation, Journal of Nuclear Materials. 510 (2018) 297–311. https://doi.org/10.1016/j.jnucmat.2018.07.060.

[47] J. Hure, A. Courcelle, I. Turque, A micromechanical analysis of swelling-induced embrittlement in neutron-irradiated austenitic stainless steels, Journal of Nuclear Materials. 565 (2022) 153732. https://doi.org/10.1016/j.jnucmat.2022.153732.

[48] S.J. Zinkle, P.J. Maziasz, R.E. Stoller, Dose dependence of the microstructural evolution in neutron-irradiated austenitic stainless steel, Journal of Nuclear Materials. 206 (1993) 266–286. https://doi.org/10.1016/0022-3115(93)90128-L.

[49] P. Dubuisson, Le gonflement des aciers austénitiques, Rev. Metall. 108 (2011) 33–37. https://doi.org/10.1051/metal/2010019.

[50] K. Ma, B. Décamps, A. Fraczkiewicz, T. Jourdan, F. Prima, M. Loyer-Prost, Free surface impact on radiation damage in pure nickel by in-situ self-ion irradiation: can it be avoided?, Acta Materialia. 212 (2021) 116874. https://doi.org/10.1016/j.actamat.2021.116874.

[51] P.J. Maziasz, Void swelling resistance of phosphorus-modified austenitic stainless steels during HFIR irradiation at 300–500°C to 57 dpa, Journal of Nuclear Materials. 200 (1993) 90–107. https://doi.org/10.1016/0022-3115(93)90013-O.

[52] P.J. Maziasz, Temperature dependence of the dislocation microstructure of PCA austenitic stainless steel irradiated in ORR spectrally-tailored experiments, Journal of Nuclear Materials. 191–194 (1992) 701–705. https://doi.org/10.1016/0022-3115(92)90563-Z.

[53] D. Gilbon, L. LeNaour, C. Rivera, H. Lorant, Effect of Irradiation Temperature on the Precipitation in Cold-Worked Titanium-Stabilized Type 316 Stainless Steel, Effects of Radiation on Materials, Proc. 12th Int. Symp., ASTM-SIP 870, Eds. F.A. Garner and J.S. Perrin. (1985) 115.

[54] P. Mukherjee, A. Sarkar, M. Bhattacharya, N. Gayathri, P. Barat, Post-irradiated microstructural characterisation of cold-worked SS316L by X-ray diffraction technique, Journal of Nuclear Materials. 395 (2009) 37–44. https://doi.org/10.1016/j.jnucmat.2009.09.013.

[55] J.F. Nye, Some geometrical relations in dislocated crystals, Acta Metallurgica. 1 (1953) 153–162. https://doi.org/10.1016/0001-6160(53)90054-6.

[56] C. Moussa, M. Bernacki, R. Besnard, N. Bozzolo, About quantitative EBSD analysis of deformation and recovery substructures in pure Tantalum, IOP Conf. Ser.: Mater. Sci. Eng. 89 (2015) 012038. https://doi.org/10.1088/1757-899X/89/1/012038.

[57] W. Pantleon, Resolving the geometrically necessary dislocation content by conventional electron backscattering diffraction, Scripta Materialia. 58 (2008) 994–997. https://doi.org/10.1016/j.scriptamat.2008.01.050.

[58] P.J. Konijnenberg, S. Zaefferer, D. Raabe, Assessment of geometrically necessary dislocation levels derived by 3D EBSD, Acta Materialia. 99 (2015) 402–414. https://doi.org/10.1016/j.actamat.2015.06.051.

[59] C.H. Woo, B.N. Singh, Production bias due to clustering of point defects in irradiation-induced cascades, Philosophical Magazine A. 65 (1992) 889–912. https://doi.org/10.1080/01418619208205596.

[60] K. Urban, Growth of defect clusters in thin nickel foils during electron irradiation (I), Phys. Stat. Sol. (a). 4 (1971) 761–772. https://doi.org/10.1002/pssa.2210040321.